Deposited via The University of Sheffield.

White Rose Research Online URL for this paper:
https://eprints.whiterose.ac.uk/id/eprint/236863/

Version: Published Version

Article:

Research article

Synthesis of cerium, zirconium, and copper doped zinc oxide nanoparticles as potential biomaterials for tissue engineering applications

Hafsah Akhtar [a,b,*], Fahad Hussain Alhamoudi [c], Julie Marshall [a], Thomas Ashton [d], Jawwad A. Darr [d], Ihtesham Ur Rehman [e], Aqif Anwar Chaudhry [b], Gwendolen Reilly [a,**]

[a] Department of Materials Science and Engineering, Pam Liversidge Building, Mappin Street, Sheffield, United Kingdom
[b] Interdisciplinary Research Centre in Biomedical Materials (IRCBM), COMSATS University Islamabad, Lahore Campus, Pakistan
[c] Dental Technology Department, Applied Medical Science, King Khalid University, Abha 62529, Kingdom of Saudi Arabia
[d] University College London, United Kingdom
[e] Research and Enterprise, School of Medicine, University of Central Lancashire, Preston, United Kingdom

ABSTRACT

A novel eco-friendly high throughput continuous hydrothermal flow system was used to synthesise phase pure ZnO and doped ZnO in order to explore their properties for tissue engineering applications. Cerium, zirconium, and copper were introduced as dopants during flow synthesis of ZnO nanoparticles, Zirconium doped ZnO were successfully synthesised, however secondary phases of CeO and CuO were detected in X-ray diffraction (XRD). The nanoparticles were characterised using X-ray diffraction, Brunauer-Emmett-Teller (BET), Dynamic Light scattering Measurements, Scanning Electron Microscopy (SEM), Transmission Electron Microscopy (TEM), Fourier transform infrared spectroscopy (FT-IR) and RAMAN spectroscopy was used to evaluate physical, chemical, and structural properties. The change in BET surface area was also significant, the surface area increased from 11.35 (ZnO_2) to 26.18 (ZrZnO_5). However. In case of CeZnO_5 and CuZnO_5 was not significant 13.68 (CeZnO_5) and 12.16 (CuZnO_5) respectively. Cell metabolic activity analysis using osteoblast-like cells (MG63) and human embryonic derived mesenchymal stem cells (hES-MP) demonstrated that doped ZnO nanoparticles supported higher cell metabolic activity compared to cells grown in standard media with no nanoparticles added, or pure zinc oxide nanoparticles. The ZrZnO_5 demonstrated the highest cell metabolic activity and non-cytotoxicity over the duration of 28 days as compared to un doped or Ce or Cu incorporated nanoparticles. The current data suggests that Zirconium doping positively enhances the properties of ZnO nanoparticles by increasing the surface area and cell proliferation. Therefore, are potential additives within biomaterials or for tissue engineering applications.

* Corresponding author. University of Sheffield, United Kingdom.
** Corresponding author.
   E-mail addresses: hafsahakhtar@cuilahore.edu.pk (H. Akhtar), g.reilly@sheffield.ac.uk (G. Reilly).

1. Introduction

The field of biomaterial and tissue engineering continuously offers novel treatment options for augmentation or regeneration of lost or damaged tissue. There is a need for improved materials which can reduce the cost and time of healing along with minimal or no side effects. Nanobioceramics are quite popular as they exist in several morphologies and sizes (sizes from μm to nm). The most common morphologies include thin sheets, nanorods, nanowires, nanobelts, nanotubes, nano-rings, flower like, multi-pods and tetra-pods. These different types of nanobioceramics can be obtained using different synthesis techniques such as hydrothermal, sono-chemical, wet chemical or solgel and can be used as granules, coatings, fillers or substitutes [1–7]. The microstructure of ceramics is an important factor in almost all biomedical applications as it affects the implant integration [8–10].

Cell adhesion, protein interaction, biocompatibility, cytocompatibility, bacteriostatic properties, angiogenesis, improved mechanical strength are all important properties for a biomaterial or a tissue engineering construct. Zinc Oxide (ZnO) is a known biomaterial, generally recognised as safe (GRAS) by US FDA for its use in food additives and skin care products. The ability of ZnO to induce reactive oxidative species (ROS) production makes it favourable for antibacterial and angiogenic applications. ZnO as a material has been explored in a number of studies for its potential anti-inflammatory, antibacterial, angiogenic applications but the literature so far still lacks the evidence based critical analysis for its use as therapeutic additive in tissue engineering applications.

Zinc is naturally present in the body and plays an important role in synthesis of several proteins and nucleic acids required for normal functioning of the body. A few studies on doped zinc oxides have reported strong angiogenic potential when introduced in a scaffold, such as potassium doped ZnO, which was used in hydrogels and resulted in neovascularisation [11]. Cerium (Ce), Zirconium (Zr) and Copper (Cu) are emerging elements in tissue engineering due to biological properties relevant for use in implants. ZnO is a popular biomaterial for its biocompatibility and cytocompatibility (Colon et al., 2006). The cerium doped bioactive glass scaffold have been reported to increase *in vitro* bioactivity hence making it favourable for bone growth and repair [12,13]. Cu is a known proangiogenic metal and also improves the biodegradation and stability of composite materials in *vitro*. Zr on the other hand is important for mechanical properties such as toughness and corrosion resistance [14].

Doping of these elements into zinc oxide is not new and has been reported for the applications of photocatalysis and photoluminance studies. A few studies concluded that there was improvement of ZnO nanoparticle properties with respect to particle size, bandgap and surface area [15]. Cerium doping resulted in enhanced ionic and ferroelectric properties [15] and have been used to detect acetone and ethanolamine levels in breath at room temperature. The study reported its use as a biomarker/biosensor for early detection of diabetes mellitus and cancer [16], detection of hazardous chemicals [17], enhanced optical and photoelectrochemical properties [18,19] and efficient photocatalysts [20]. The cerium doping or substitution resulted in reduced grain size, increased bandgap and lattice expansion of ZnO [15,16].

Similarly, copper doped ZnO enhanced the electrical properties of ZnO and resulted in uniform grain size [21]. Zirconium doping resulted in improved mechanical properties [22]. ZnO is a known biomaterial and has been reported to improve cell adhesion & proliferation in bone tissue regeneration and applications that require good blood vessel formation (angiogenesis). The doped ZnO nanoparticles' synthesis have been reported in literature, however, the properties of doped ZnO as a biomaterial have not been evaluated. In this study, functional modification of ZnO was performed by doping metals such as Ce, Zr and Cu, the purpose was to improve the cell adhesion and proliferation of ZnO nanoparticles. The study was performed to utilise the existing biological properties of the ZnO and further improve it using different ionic dopings. The ionic doped ZnO nanoparticles were explored for their potential use in biomaterial and tissue engineering applications in the future.

Three types of doped ZnO were prepared; Ce doped ZnO, Zr doped ZnO and Cu doped ZnO respectively, in varying concentrations. The resultant doped ZnO nanoparticles are novel and have been synthesised using a novel high throughput continuous hydrothermal flow system. The properties of zirconium, copper and cerium doped zinc oxide nanoparticles were evaluated as a potential candidate for bone biomaterial applications. The surface area, particle morphology and size were evaluated, and cell metabolic activity analysis was performed to explore the effect of doping on cell growth in comparison to phase pure ZnO as control. A secondary aim of the study was to identify if cerium, zirconium, or copper doped ZnO have any cytotoxic effects short term (over the duration of 7 days) and long term (28 days). This is the first study reporting the metabolic activity of cells exposed to doped zinc oxide nanoparticles and relevant properties which might be useful in future for the use of these doped ZnO nanoparticles for potential applications in tissue engineering and regenerative medicine.

2. Materials and methods

2.1. Materials

Zinc nitrate hexa hydrate ($Zn(NO_3)_2.6H_2O$), Potassium hydroxide (KOH), Cerium (III) Nitrate hexahydrate 99.5%, Zirconyle (IV) Nitrate hydrate 99.5%, Copper (III) Nitrate hemi(pentahydrate) $Cu(NO_3)_2.2H_2O$ 99.9% (ACROS Organics), Hydroxyapatite commercial grade (Finceramica) were used as received. Cell culture media DMEM and Alpha MEM for MG63 and hES-MP cell lines. Trypsin-EDTA, Penicillin streptomycin and FBS were supplied by Sigma-Aldrich.

2.2. ZnO and doped ZnO nanoparticles synthesis

The concentrations within precursor solutions were adjusted to obtain two groups of nanoparticles, the aim was to obtain different particle sizes with the same chemistry. For group 1 nanoparticles, the precursor solution concentrations were 0.2 M KOH and O.1 M

zinc nitrate and for group 2 the 1 M KOH and 0.5 M zinc nitrate solution were used. Table 1 shows the concentrations of precursor solution and dopants used. To synthesise doped zinc oxides, pre-weighed dopant sources [Ce(NO₃)₃.6H₂O, copper nitrate and zirconium nitrate] were added to zinc nitrate solution under continuous stirring.

The precursor solutions prepared at room temperature were pumped through pumps 2 and Pump 3 (Fig. 1)(flow rate: 40 ml/min). The solutions were pumped through Polytetrafluoroethylene (PTFE) tubing which was connected with a 3/4inch SS-316L T-piece, serving as reaction mixer. The mixture was pumped to the reaction centre (R) where it came into contact with supercritical water which acted as the crystallisation medium. The zinc salts were converted into zinc oxides due to rapid hydrolysis and dehydration. The resultant product was cooled to 40 °C by passing through a pipe in the cooling chamber. The cooled product or slurry was then passed through back pressure regulator (BPR) to maintain the pressure in the system. The nanoparticles were obtained in the form of a slurry, in a beaker at 25 °C. The slurry was washed twice with deionized water and freeze dried (Virtis Genesis 35XL) by slowly heating the samples from −60 °C to 25 °C for 24 h at vacuum of <13.3 Pa to obtain nanopowders.

2.3. Dynamic Light scattering measurements (DLS)

DLS was used to obtain the hydrodynamic diameter of the nanoparticles using a Zeta Ziser Nanoseries machine. The nanoparticles were sonicated in 1 ml deionized water for 5min and analysed. The measurements were performed three times and a mean was calculated.

2.4. X-ray diffraction (XRD)

Brukner D2 Phaser was used to perform the analysis. The parameters used were total effective time 310.8 s, time 0.600 s, 2 theta 30–80, voltage 30 and current 10. The parameters were same for all the samples.

2.5. Raman spectroscopy

Raman characterisation was performed using Raman DXR Xi. The Raman spectra were obtained using laser 780 nm and Aperture 25 μm. The scan range was selected from 100 cm^{-1} to 4000 cm^{-1}.

2.6. FTIR spectroscopy

The FTIR spectrum was collected using a Thermo Fischer scientific (Nicolet 6700TM) spectrophotometer. The smart iTR diamond ATR (Attenuated Total Reflectance) mode at resolution of 8 cm^{-1} was used to obtain a total of 256 scans within a range of 4000–500 cm^{-1}.

2.7. Brunauer-Emmett-Teller (BET)

Physical Adsorption isotherms of N₂ at −196 °C were measured by Tristar II Micrometrics. All the samples were degassed under N₂

Table 1
The concentrations of precursor solutions and dopant quantities used to synthesise ZnO, cerium doped ZnO, zirconium doped ZnO and copper doped ZnO.

| NAMES	[KOH]	[Zn]*	M precursor	[M]	Volume (L)	Mass Zn* (g)	Mass (g)
ZnO_1	0.2	0.1	N/A	0	1	29.75	0.00
ZnO_2	1	0.5	N/A	0	0.5	74.37	0.00
ZrZnO_1	0.2	0.099	ZrO(NO₃)².6H₂O	0.001	1	29.45	0.30
ZrZnO_2	0.2	0.097	ZrO(NO₃)².6H₂O	0.003	1	28.85	0.89
ZrZnO_3	0.2	0.095	ZrO(NO₃)².6H₂O	0.005	1	28.26	1.49
ZrZnO_4	1	0.495	ZrO(NO₃)².6H₂O	0.005	0.5	73.62	0.74
ZrZnO_5	1	0.485	ZrO(NO₃)².6H₂O	0.015	0.5	72.14	2.23
ZrZnO_6	1	0.475	ZrO(NO₃)².6H₂O	0.025	0.5	70.65	3.72
CeZnO_1	0.2	0.099	Ce(NO₃)³.6H2O	0.001	1	29.45	0.43
CeZnO_2	0.2	0.097	Ce(NO3)3.6H₂O	0.003	1	28.85	1.30
CeZnO_3	0.2	0.095	Ce(NO3)3.6H₂O	0.005	1	28.26	2.17
CeZnO_4	1	0.495	Ce(NO3)3.6H₂O	0.005	0.5	73.62	1.09
CeZnO_5	1	0.485	Ce(NO3)3.6H₂O	0.015	0.5	72.14	3.26
CeZnO_6	1	0.475	Ce(NO3)3.6H₂O	0.025	0.5	70.65	5.43
CuZnO_1	0.2	0.099	Cu(NO₃)².3H₂O	0.001	1	29.45	0.24
CuZnO_2	0.2	0.097	Cu(NO₃)².3H₂O	0.003	1	28.85	0.72
CuZnO_3	0.2	0.095	Cu(NO₃)².3H₂O	0.005	1	28.26	1.21
CuZnO_4	1	0.495	Cu(NO₃)².3H₂O	0.005	0.5	73.62	0.60
CuZnO_5	1	0.485	Cu(NO₃)².3H₂O	0.015	0.5	72.14	1.81
CuZnO_6	1	0.475	Cu(NO₃)².3H₂O	0.025	0.5	70.65	3.02
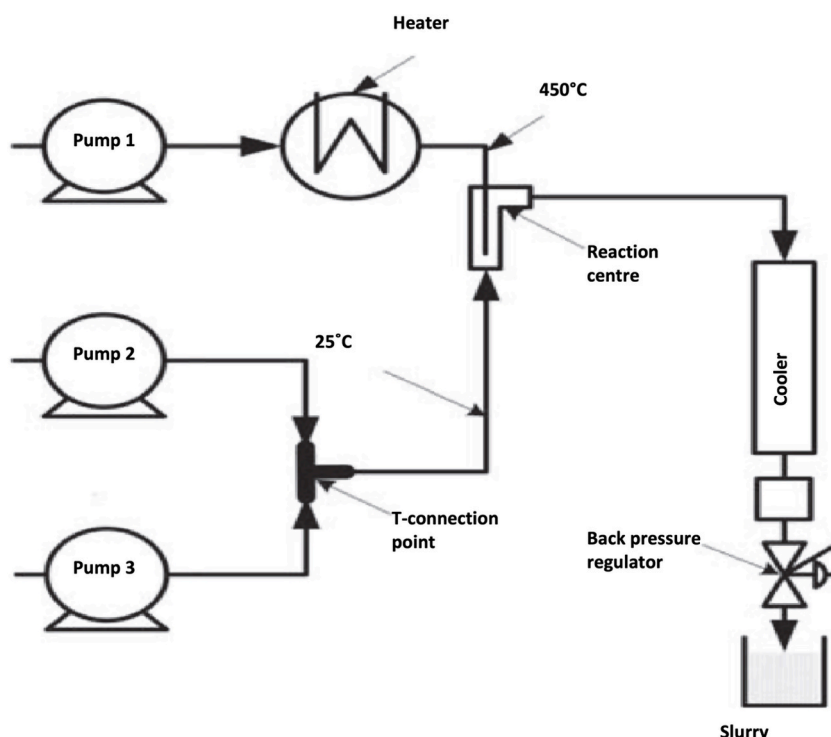
Fig. 1. Schematic diagram of hydrothermal flow system.

at 150 °C for 12 h before BET surface area from N_2 isotherms were measured. The measurements were performed at 10 points.

2.8. Scanning electron microscopy

The morphology of Nano powders was investigated using scanning electron microscopy Vega 3 LMU – TESCAN. The nanopowders were suspended in absolute ethanol using a sonicator followed by dropping 100 µl on a SEM stub. The stubs were left for ethanol evaporation for 5 min followed by gold coating with a thickness of 250 Å using a coating unit.

2.9. Transmission Electron Microscopy (TEM)

The nanoparticles were suspended in absolute ethanol and sonicated for 2 h. The 10 µl sample was dropped onto discharged copper palladium carbon-coated TEM grids and left to dry for 10 min. The excess ethanol was removed carefully using clean filter paper (Whatman grade 1 GE HealthCare UK, Little Chalfont, UK). The prepared TEM grids were visualised using a FEI Tecnai G2 Biotwin Tranmission Electron Microscope (FEI Cambridge, UK) at 80kv voltage. Micrographs were obtained using a Gatan Orius 1000B digital camera and software suite (Gatan Ltd, Corby UK).

2.10. Cell metabolic activity assay of nanoparticles

Sterilisation of Nanoparticles: 2000 µg nanoparticles were weighed on an electronic balance and stored in Eppendorf tubes. The Eppendorf tubes were autoclaved at 121 °C for 30 min to sterilize the nanoparticles. 2000 µl of media without serum (DMEM for MG63 and Alpha MEM for hES-MPs) was added to the eppendorf tubes in a cell culture hood. The Eppendorf tubes were then sonicated at room temperature for 30 min to create homogenous suspensions. The stock suspension was created in a way that 1 µl contained 2 µg of nanoparticles. The working solutions were prepared by taking the desired amount of stock solution and diluting it into serum free media in a sterile environment (Table 2).

Table 2
The nanoparticle suspension preparation from stock solution for cell metabolic activity assay.

Desired concentration	Required suspension quantity	Suspension quantity stock solution	Amount of serum free media (DMEM or Alpha MEM)
5 µg/ml	100 µl	2.5 µl	97.5 µl
10 µg/ml	100 µl	5 µl	95 µl

Working solutions were prepared in serum free DMEM or Alpha MEM.

Cell seeding for cell metabolic activity assay (MG63 cell line): This assay is a semi quantitative assay to determine cell metabolic activity overall in the culture well, the output obtained is an indicator of cell number assuming that the metabolic activity per cell remains the same and is not affected by the test samples. The MG63 cell line was used for the cell metabolic activity assessment for 7 days. Cells were cultured and maintained at 37 °C and 5% CO_2 with Dulbecco's modified eagle's medium (DMEM) supplemented with 10% FBS (Advanced protein products, Brierley Hill, UK), 100 IU/mL penicillin, 100 μg/mL streptomycin, 2 mM glutamine, and 0.25% fungizone (Gibco Invitrogen, Paisley, UK).

1×10^4 cells per ml was seeded into 24 well plates, the cells were allowed to attach for 24 h followed by addition of nanoparticle suspension. Two concentrations of nanoparticle suspension were tested; 5 μg/ml and 10 μg/ml. A resazurin assay was performed at culture days 1,3,5 and 7. At the assay time-points the resazurin assay was performed to measure the absorbance of reduced resazurin. The cell culture media or nanoparticle suspension was re-introduced and well plates were returned to the CO_2 incubator.

2.11. 28 Day cell metabolic activity assay using hES-MPs

The Human Embryonic mesenchymal like stem cells hES-MPs were for 28 day cell metabolic activity assessment. 1×10^4 cells per ml per well were seeded. After cell attachment 10 μg/ml nanoparticle suspension was added to each well for by the replacement of nanoparticle suspension every two days. The resazurin assay was performed at Day 7, Day 14, Day 21 and Day 28. Microplate reader was used to record fluorescence values.

Statistical Analysis: The experiments were conducted in triplicate and repeated three times (n = 3 and N = 3). Data sets are reported as mean ± standard deviation. Comparison of sample means of resazurin absorbance data was performed by two-way analysis of variance using GraphPad Prism. Differences between two groups were distinguished as statistically significant if $p \leq 0.05$ (*), $p \leq 0.01$ (**), $p \leq 0.001$ (***) and $p \leq 0.0001$ (****) as determined by the Turkey post-hoc test.

3. Results and discussion

3.1. Dynamic Light scattering (DLS) for hydrodynamic diameter measurements

The hydrodynamic diameter was within a range between 21 nm and 113.8 nm and with varying concentrations of precursor solutions i.e., potassium hydroxide and zinc nitrate led to notable differences in hydrodynamic diameter size. But a less notable difference was observed when samples were introduced with cerium, copper, and zirconium. Furthermore, it was observed that increasing the dopant amount led to bigger hydrodynamic diameter (Table 3).

3.2. Brunauer–Emmett–Teller (BET)

The preliminary DLS findings were further confirmed by using BET surface area analysis. The change in precursor solution concentration led to significant increase in surface area in the case of pure zinc oxide, but for doped zinc oxide only marginal increase in surface was observed (Table 3).

Table 3
The physical characterisation data of synthesised nanoparticles. n = 3.

	Sample name	Hydrodynamic diameter (nm)	BET surface area m2/g	Crystallite size (Scherrer equation) (nm)	Average particle size (calculated from TEM imaging) (nm) (+S.D 22.87 nm)
1	ZnO_1	21.02	6.76	32.35	83.16
2	ZnO_2	134.50	11.35	31.70	45.23
3	CeZnO_1	100.70	15.64	31.38	88.45
4	CeZnO_2	88.88	12.88	32.45	67.30
5	CeZnO_3	101.70	13.68	31.41	49.88
6	CeZnO_4	70.49	12.32	31.23	79.21
7	CeZnO_5	98.95	13.68	31.30	51.67
8	CeZnO_5	103.3	14.03	32.32	50.08
9	ZrZnO_1	87.06	16.99	29.04	43.32
10	ZrZnO_2	99.74	24.44	25.78	42.30
11	ZrZnO_3	113.8	29.07	29.12	73.50
12	ZrZnO_4	103.4	16.11	31.21	49.55
13	ZrZnO_5	98.3	26.18	31.20	54.39
14	ZrZnO_6	91.34	29.84	32.36	58.16
15	CuZnO_1	64.82	11.86	30.11	51.21
16	CuZnO_2	74.82	11.66	32.35	50.61
17	CuZnO_3	83.83	12.30	30.53	60.01
18	CuZnO_4	94.97	11.05	30.11	57.54
19	CuZnO_5	55.21	12.16	29.11	51.74
20	CuZnO_6	83.83	13.46	30.1	53.37

3.3. X-ray diffraction analysis (XRD)

The ZnO samples were matched to PDF 00-036-1541 which confirmed the successful synthesis of pure zinc oxide. The diffraction pattern showed very sharp peaks which indicated the high crystallinity and hexagonal wurtzite crystal structure of the sample [23,24].

The addition of cerium resulted in the appearance of a signal at 33° which was attributed to cerium oxide (CeO_2) (Fig. 2), after matching with the PDF 00-067-0123 [25]. At lower cerium concentration (CeZnO_1), a very weak signal at 33° was recorded which became more evident as the cerium concentration was increased (CeZnO_2 & CeZnO_3) (Fig. 2). A similar pattern was observed in other cerium group (CeZnO_4, CeZnO_5 & CeZnO_6). The sharpness of the peaks remained the same even after doping which confirmed good crystallinity. The peak at 47.5° resulted in increased intensity with an increase in cerium content. This peak is associated with the zinc oxide & CeO_2 lattices, which demonstrated the change in geometry of the overall crystal structure. PDF 00-067-0123 matching demonstrated the cubic fluorite like structure. The increase in intensities of the peak at 33° associated with CeO_2 confirmed the presence of two phases; hexagonal and cubic (ZnO & CeO_2) (Fig. 2) [24,25]. The crystallite/grain size was observed to be almost the same for all the samples, no significant change in size was observed with variations in precursor concentrations or doping concentrations (Table 1).

The Zirconium doped ZnO nanoparticles indicated high crystallinity similar to hexagonal wurtzite zinc oxide (Fig. 3). No oxide or any other phases were observed. This indicated either there is a very low quantity of secondary phase that cannot be detected or that the Zirconium doping is present in the form of an impurity in the zinc oxide lattice. However, the increase in zirconium content led to a shift of the spectra slightly, to the lower angle. This effect was associated with the increased ionic size of Zr^{+4} compared to Zn^{+2}, upon substitution Zr^{+4} crystal lattice distortion likely happened which resulted in reduced particle size as the zirconium content was increased (Table 3). The peak shift to a lower angle as the concentration (Fig. 3) was increased confirmed the substitution of Zr into the zinc oxide [26]. This shift indicated the presence of zirconium as an impurity, introduction of zirconium to zinc oxide caused the expansion of the zinc oxide lattice due to ionic radii mismatch [26,27]. Another possible reason for the lack of zirconium peaks can be that zirconium ions are completely trapped by the zinc oxide lattice, hence making it difficult for the diffractometer to detect it as another entity [28]. The widening or broadening of the peak was not observed in resultant nanoparticles which indicated the high crystallinity of the zirconium doped zinc oxide nanoparticles, as suppression of nanoparticle crystallinity is indicated by less intense or broad peaks [29]. There was again no difference in crystallite size calculated, however previous studies have shown a reduction in crystallite size upon increase in zirconium content. In our experiments, the difference is not evident, which might be because of a small change in dopant percentages (from 1% to 5%) [30,31]. A slight decrease however was recorded when the percentage was increased from 1% to 3%, which is associated with the incorporation of zirconium ions in the lattice.

Likewise, sharp peaks were observed of Cu doped zinc oxide also, which confirmed the high crystallinity. The CuZnO_1 diffraction pattern was found to be similar to the zinc oxide. The characteristic peaks were observed at an angle 2 theta i.e., at 31.78°, 34.43°, 36.25°, 47.57°, 56.63° and 62.89° which correspond to the Miller Indices (100, 002, 101, 102, 110 and 103) are related to the standard hexagonal wurtzite crystal structure of zinc oxide NPs (PDF 00-036-1541). This indicated a very low quantity of secondary phase that cannot be detected. However, at higher copper concentrations another peak was detectable. The new phase was matched to PDF 00-048-1548 which was denoted to CuO (Fig. 4) [32]. The data confirmed the incorporation of CuO in the zinc oxide, as the particle size
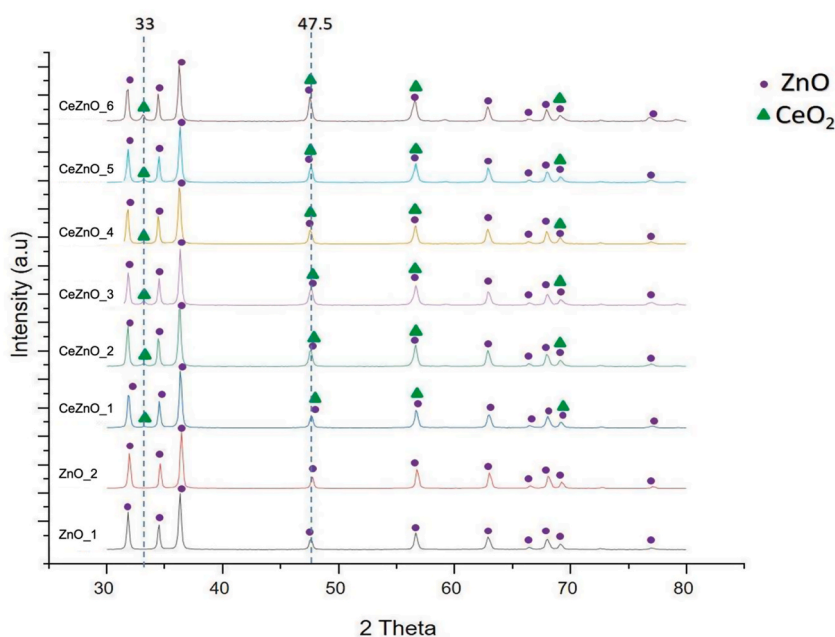

Fig. 2. Change in crystal properties of ZnO and appearance of CeO_2 at different amounts of cerium content.
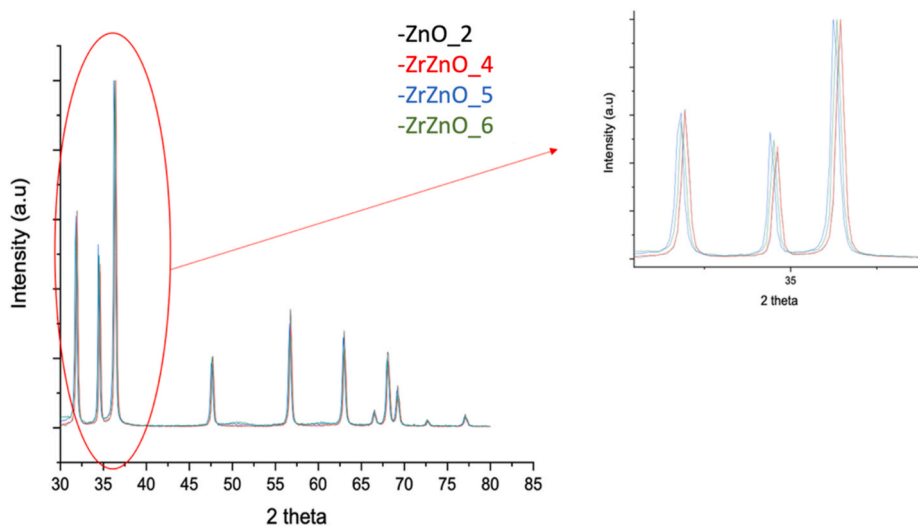
Fig. 3. The XRD peak shift due to Zirconium incorporation into the zinc oxide lattice during the synthesis process.
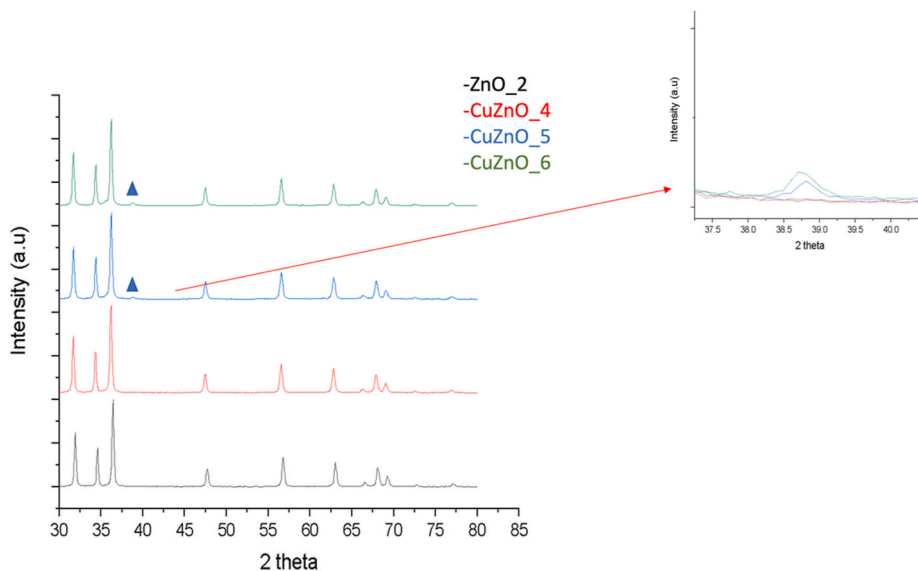

Fig. 4. The appearance of another phase due to copper incorporation during the synthesis process is shown in this XRD pattern.

decreased the concentration of Cu increased. This pattern of smaller particle size with higher Cu can be seen by comparing CuZnO_4, CuZnO_5 and CuZnO_6, the size decreased from 96.82 nm in CuZnO_4, to 87.94 nm in CuZnO_5 and 79.47 nm in CuZnO_6(Table 3). This confirms a trend previously reported in literature [33]. The reason for the reduced particle size is linked with the coating of CuO over zinc oxide given that CuO has a smaller size, compared to zinc oxide [34]. Zinc oxide and CuO were the only phases observed and the indices indicated the formation of a phase pure CuO/zinc oxide [35]. The sharp peaks for all the samples depicted the high crystallinity of the nanopowders [32]. And also lower Cu concentration corresponding to a tenorite-like oxide (ZnxCu1−xO) phase

Table 4
The structural parameters of ZnO and doped ZnO derived from FTIR data.

Wavelength (cm^{-1})	Attribution	Reference
3701–2482	O–H stretching vibration	[41]
1051	attributed to stretching vibrations H–O–H	[42]
670–640	Vibrational energies of Zn–O	[43]
1051–960	NO$_3$ $^{-1}$	[44,45]
1385, 1514	CO	[44,45]

[36,37].

3.4. Fourier transform infrared spectroscopy

The FTIR spectra demonstrated the presence of signature peaks for ZnO in all samples as shown in Table 4. The broad band at 3701-2482 cm^{-1} demonstrated the presence of H_2O in nanocrystals of ZnO or doped ZnO (Fig. 5 A-D). The characteristic peaks corresponding to vibrational energies of Zn–O at 620 cm^{-1} and 680 cm^{-1} were found in all samples (Table 4) [38]. No other absorption band was detected in the FT-IR spectrum indicating that the synthesised nanoparticles are pure (Fig. 5 A-D) [39,40].

3.5. Raman spectral analysis

Live Raman spectral analysis was performed at room temperature to investigate the Raman scattering of zinc oxide nanoparticles and the influence of Cerium doping on characteristic zinc oxide Raman scattering. Zinc oxide synthesised via Hydrothermal flow was characterised as wurtzite (crystal structure having hexagonal unite cell), zinc oxide because of the presence of eight characteristic optical phonon modes at the centre of Brillouin Zone (Γ point). Fig. 6 represents room temperature Raman spectra of pure zinc oxide. Γ = 1A1 + 2B1 + 1E1 + 2E2.

The spectra demonstrated the four characteristic peaks at 100, 380, 437 and 580 cm-1 which are characteristic phonon modes of hexagonal zinc oxide. The peaks were characterised as E2L, A1(TO), E2H, and A1(LO) respectively.

A1, E1 and E2 were characterised as Raman active modes. A_1 and E1 were categorised as polar branches. The polar branches divide into longitudinal Optical (LO) and transversal optical components which were associated with different frequencies due to LO phonons associated electric fields. The E_2 Raman nonpolar mode associated with low frequency was classified as E_{2L} which depicted a heavy Zn sub lattice. However, nonpolar high frequency mode E_{2H} only involved oxygen atoms.

The spectra demonstrated the appearance of Raman active mode F_{2g} (Fig. 7) which is the characteristic peak for the CeO_2 cubic structured lattice. The remaining peaks associated with the zinc oxide hexagonal structure were found at the same position. The F_{2g} corresponded to a ceria (CeO_2) vibrational unit which shows the oxidation of Ce^{3+} during hydrothermal synthesis. This confirmed the presence of two phases in the sample zinc oxide and CeO_2 respectively [23].

Cerium Oxide (CeO_2) belongs to the group of cubic fluorite structures. In samples in which cerium was introduced into zinc oxide, the first order Raman active phonon mode F_{2g} appeared as shown in Fig. 7 with reduced amounts of cerium there (Fig. 7) there was no longer evidence of the Raman characteristic peak of zinc oxide at 380 cm −1 A_1(TO) which is one of three characteristic vibration modes of wurtzite zinc oxide with $P6_3mc$ symmetry (Fig. 7) [23,24,46].

ZnO_1 and ZnO_2 shows Raman spectra of pure zinc oxide, moving upwards CeZnO_1 to CeZnO_3 is one cerium group and CeZnO_4- CeZnO_6 is another cerium group having cerium content 1 mol %, 3 mol % and 5 mol % respectively (Fig. 7). As the cerium
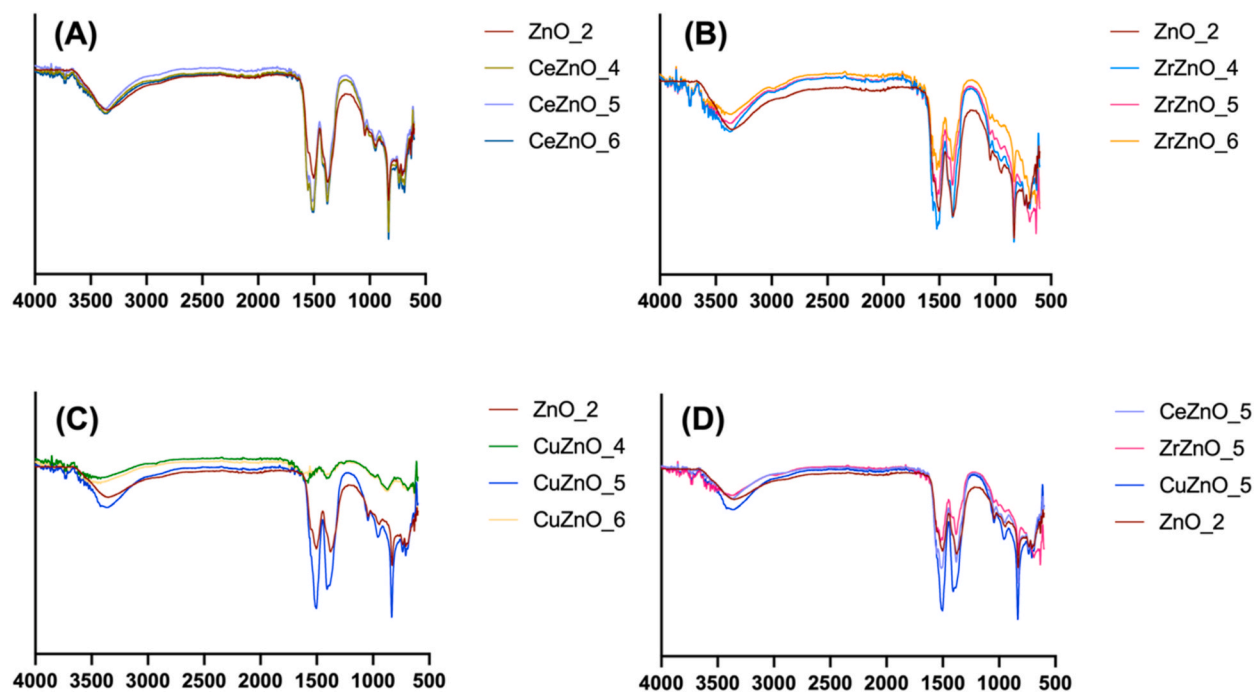

Fig. 5. FTIR spectra of cerium, zirconium and copper doped ZnO nanoparticles. A) Cerium doped ZnO, B) Zirconium doped ZnO, C) Copper doped ZnO and D) Cerium, Zirconium, copper doped ZnO & phase pure ZnO overlap for comparison.
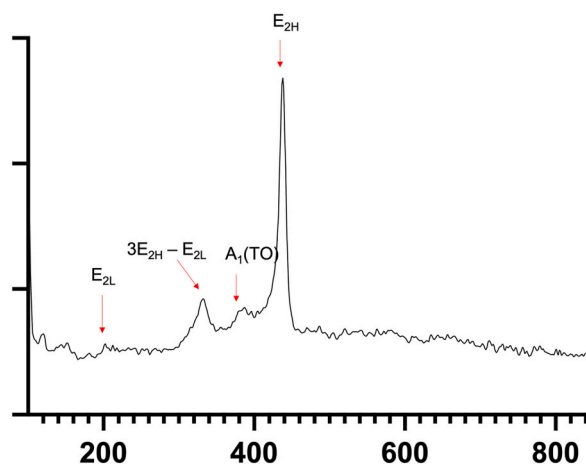
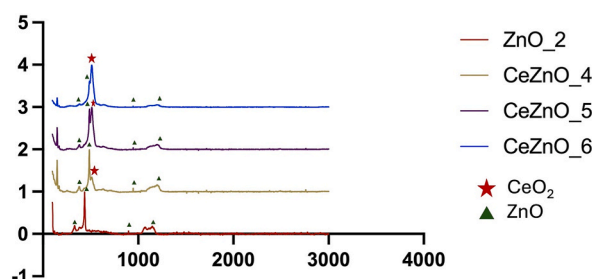**Fig. 6.** RAMAN spectra of phase pure ZnO (ZnO_2) demonstrating the characteristic ZnO peaks.

Fig. 7. RAMAN spectral analysis of CeZnO_4, CeZnO_5 and CeZnO_6 in comparison to control ZnO_2. The overlap of RAMAN spectra shows the shift of F_{2g} as the cerium concentration was increased.

content was increased the partial oxidation of Ce^{+3} happened during the hydrothermal process at 335 °C leading to formation of cubic CeO_2. It was observed that the peak intensities for characteristic wurtzite zinc oxide reduced as the cerium content was increased (shown by purple dots), however, the Raman active mode for ceria F_{2g} increased as the cerium content was increased (Fig. 7) [23].

The spectra confirmed the presence of characteristic peaks for hexagonal wurtzite ZnO crystal (A_1(TO), E_{2H} and A_1(LO)) (Fig. 8 A). The addition of Zirconium had an impact on the structure of ZnO crystals. When the comparison of pure ZnO and zirconium doped ZnO was performed, it was evident that the intensity of transverse optical mode A_1(TO) at 574 cm-1 reduced with the addition of zirconium (Fig. 8 B), however, the intensity of optical phonon mode A_1(LO) at 574 cm-1 increased with the increase in zirconium concentration [47]. The E_{2H} was intense which showed the good crystallinity mobility of oxygen atoms of both doped and pure ZnO. E_{2H} is known as signature peak for hexagonal wurtzite ZnO crystal structure [48]. The E_{2H} intensity and position did not change even after addition of zirconium which confirms the good crystallinity and hexagonal crystal structure stayed even after the doping, consistent with the XRD
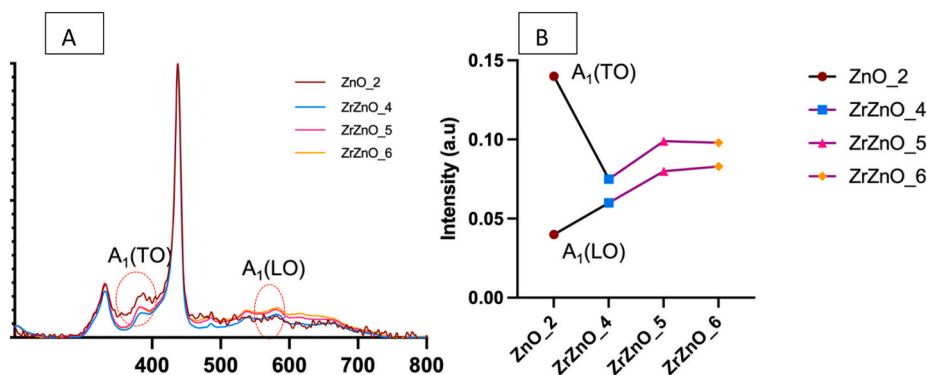
Fig. 8. *RAMAN Spectral analysis of zirconium doped ZnO. A) Overlap of zirconium doped ZnO spectra highlighting the change as the zirconium concentration was increased. B) Shows the change in intensity of A_1(TO) and A_1(LO) as the concentration of zirconium was increased.*

results. The change in peak intensities of $A_1(LO)$ and $A_1(TO)$ suggested the slight change in lattice structure of ZnO due to doping (Fig. 8 A & B). The change might be due to zirconium ions taking the place of Zinc ions at some positions in lattice structure [49]. The slight shift in XRD data confirms the same finding.

In the case of copper doped ZnO, the characteristic ZnO peak E_{2H} was observed but with reduced intensity (broad peak can be seen in Fig. 9). The E_{2H} is usually because of the vibration of oxygen atoms, demonstrating a wurtzite ZnO structure. The E_{2L}, E_{2H}-E_{2L} and $A_1(TO)$, the characteristic ZnO peaks were not quite visible in the copper doped ZnO spectra which was due to successful formation of ZnO–CuO nanoparticles. Another peak at 2330 cm^{-1} was observed in copper doped ZnO RAMAN spectra, the reason of this peak is unclear but is associated with formation of CuO [50]. The reduced peak intensity and peak broadening of E_{2H} was observed which demonstrated the low crystallinity of copper doped ZnO nanoparticles (Fig. 9) [47].

3.5.1. Scanning electron microscopy

The nanopowders formed agglomerates of several particles (Fig. 10 A-F). The samples were sonicated before SEM analysis, but particle separation was not achieved which might be due to weak physical forces. The nanoparticles were found fused together to make micron sized particles. Even at 23Kx it was difficult to evaluate the individual particle size range due to agglomeration [51]. The high level of agglomeration prevented observation of morphological differences in the SEM images of nanoparticles. However, it was possible to confirm that the size of particles is in the nano range (The zirconium doped nanoparticles SEM micrographs are shown). To study the morphology of the particles TEM was performed. Similar findings were noted to those previously reported for zirconium doping in literature [28]. The SEM micrographs of zirconium doped ZnO are shown for reference (Fig. 10 A-F).

3.6. Transmission Electron Microscopy (TEM)

It was performed to analyse the differences in physical properties of nanoparticles between doping concentrations. For pure zinc oxide, the structure was rod shaped and the size was around 100 nm–150 nm (Fig. 11 A). However, with addition of cerium content, the shape remained rod like, but the size of the rods reduced significantly. The size range for CeZnO_1 is 50 nm–100 nm (Fig. 11 B). At higher cerium content, 2 morphologies were observed (CeZnO_2), rounded particles and rod like particles (Fig. 11 C). At a further, increase in cerium content (CeZnO_3) most particles were spherical (Fig. 11 D), and size reduced (Table 3) significantly. It was concluded that the final nano powder might contain two types of particles: rod shaped zinc oxide and cubic or rounded CeO$_2$ [52].

At the lowest concentration of Zirconium doping (1%) the size of particles was lower compared to control zinc oxide nanoparticles (Fig. 12 A). Also, fewer rods were spotted in ZrZnO_1 and ZrZnO_4 (Fig. 12 A & D). As the concentration increased agglomerates of quite small particles were spotted (approximately 3.5–4 nm) (ZrZnO_2, ZrZnO_3, ZrZnO_5 and ZrZnO_6) (Fig. 12 B, C, E & F). The introduction of ions resulted in expansion of the zinc oxide lattice leading to reduced grain size and increased bandgap [15,16]. It is evident that doping resulted in change in particle size and partly the particle morphology (Table 3) (Fig. 12 A-F).

For CuZnO_1, CuZnO_2 and CuZnO_3, fewer rod like structures were visible, mostly rounded morphologies could be seen even at higher copper concentrations (Fig. 13 A-C). The second phase was not clearly visible which can be confirmed from XRD data. However, the CuZnO_4, CuZnO_5 and CuZnO_6 showed mixed morphology (Fig. 13 D-F) with both rod-like and spherical particles, which might explain the presence of the CuO phase along with rod-like zinc oxide nanoparticles (Fig. 13 F). Image J was used to evaluate the particle size. The average particle size ranged between 50 and 60 nm (Table 3).

3.7. Cell metabolic activity assay with a human osteoblast like cell line (MG63)

The 5 µg/ml (Fig. 14 A) *and* 10 µg/ml *ZnO* (Fig. 14 B) *and doped ZnO suspensions were used for cell metabolic activity assay.* The presence of ZnO_1 and CeZnO_2 improved cell metabolic activity and similarly ZnO_2 and CeZnO_5 increased cell metabolic activity which can be related to increased proliferation up to day 7. The nanoparticles were not found to be toxic nor had inhibitory effects on cell growth at the given concentrations (Fig. 14 A & B).

Similarly, cell cultures containing ZrZnO_2 and ZrZnO_5 showed the highest cell viability for up to 7 days (Fig. 15 A & B).

A similar assay was run for copper doped ZnO nanoparticles and CuZnO_2 and CuZnO_5 showed improved viability as compared to the control samples. None of the nanoparticle suspensions were found to have inhibitory or toxic effects on cells. The cells were
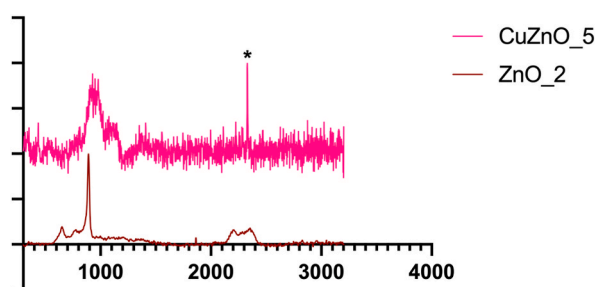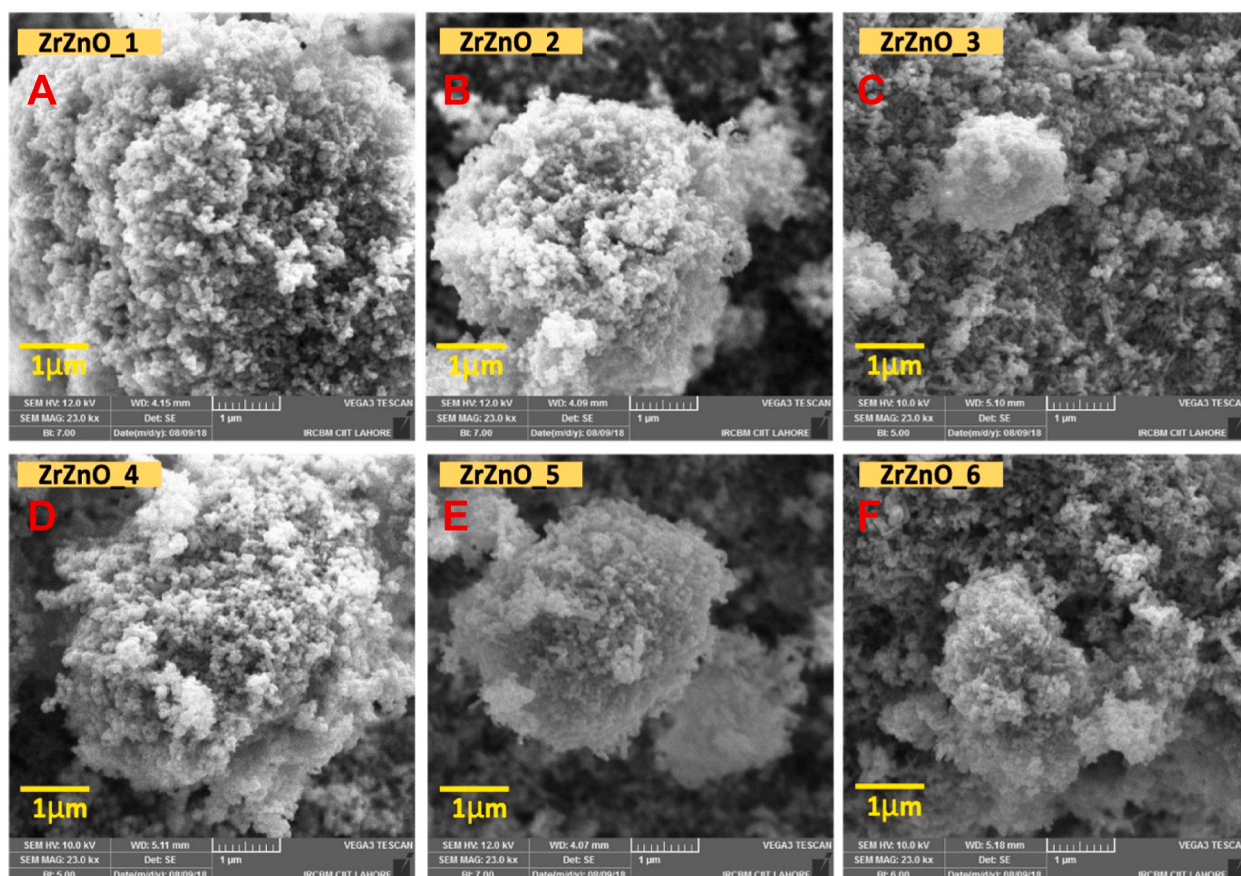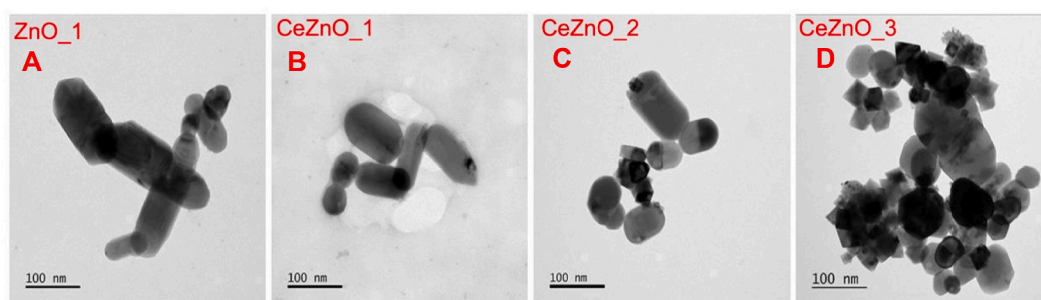

Fig. 9. RAMAN spectra CuZnO_5 compared with phase pure ZnO (ZnO_2).

Fig. 10. Scanning Electron Micrographs of agglomerates of Zirconium doped Zinc oxide nanoparticles at 23kx magnification. A) ZrZnO_1, B) ZrZnO_2, C) ZrZnO_3, D) ZrZnO_4, E) ZrZnO_5, & F) ZrZnO_6.

Fig. 11. TEM imaging of cerium doped ZnO nanoparticles. A) ZnO_1 (Control), B) CeZnO_1, C) CeZnO_2, & D) CeZnO_3.

metabolically active for the whole duration of the experiment (7 days). (Fig. 16 A & B).

3.8. 28- day cell metabolic activity assay using cells from the hES-MPs cell line (10 µg/ml nanoparticle suspension)

hES-MPs were used for a 28 day study in order to evaluate the long-term contact effect on cells and to evaluate the safety of nanoparticles using cells more representative of those used in tissue engineering. ZnO_2, CeZnO_5, ZrZnO_5 and CuZnO_5 was selected for further investigations based on nanoparticle size (ZnO_2, CeZnO_5, ZrZnO_5 and CuZnO_5 have a smaller particle size, Table 3).

At Day 1, no significant difference was seen between ZnO_2 or doped ZnO nanoparticles. The cells were attached to tissue culture plastic and no adhesion impairment was observed under the microscope. At Day 7, ZnO_2, CeZnO_5 and ZrZnO_5 improved cell metabolic activity significantly compared to the standard media control (Fig. 17 A), however no notable difference was observed between standard media control and CuZnO_5.
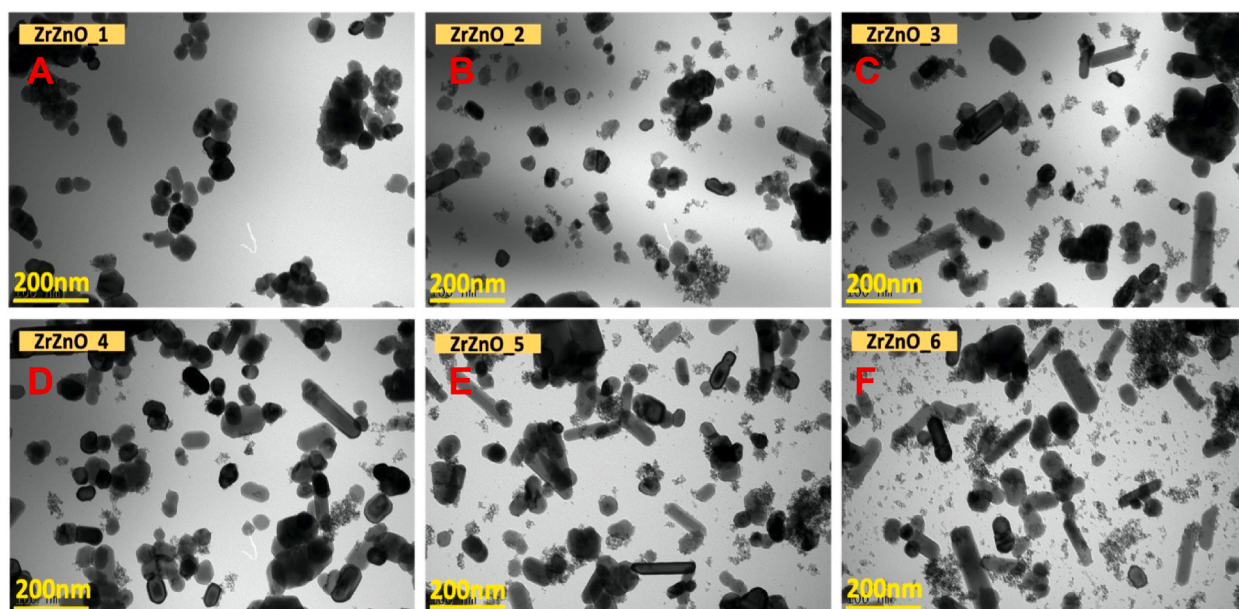
Fig. 12. Transmission Electron Micrographs revealing morphology of zirconium doped ZnO nanoparticles and effect of Zirconium doping on nanoparticle morphology with increasing percentage of zirconium. A) ZrZnO_1 B) ZrZnO_2 C) ZrZnO_3 D) ZrZnO_4 E) ZrZnO_5 & F) ZrZnO_6.
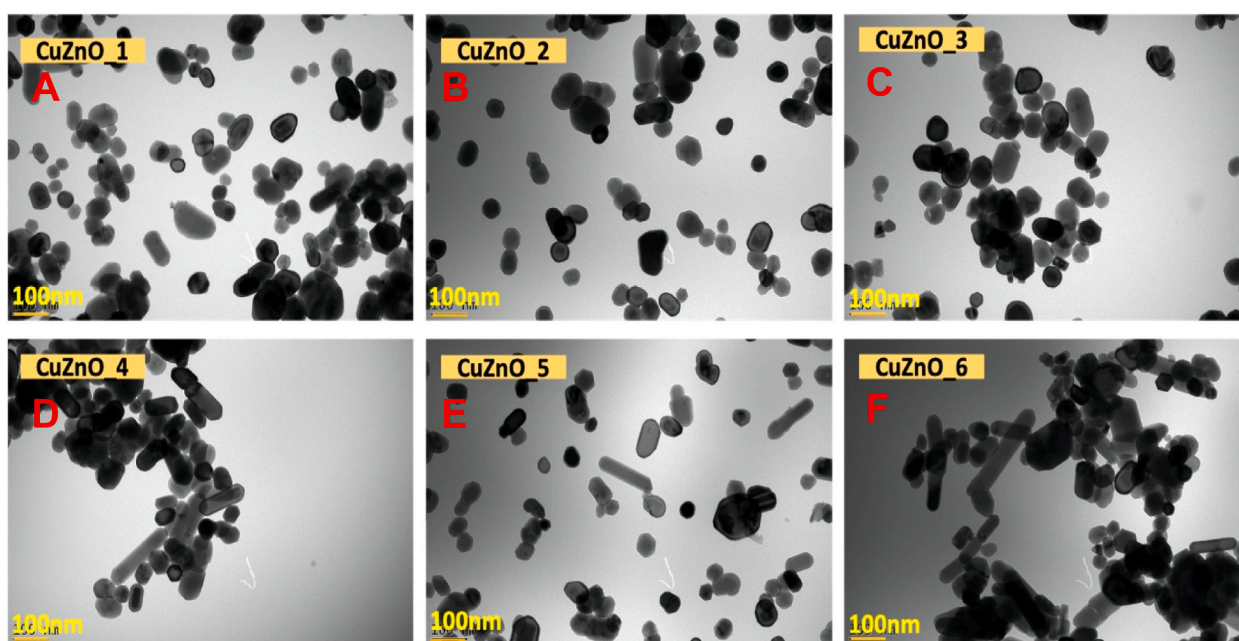
Fig. 13. Transmission Electron Micrograph of copper doped ZnO nanoparticles, at higher Copper doping agglomeration of nanoparticles is visible. A) A) CuZnO_1 B) CuZnO_2 C) CuZnO_3 D) CuZnO_4 E) CuZnO_5 & F) CuZnO_6.

From Day 14 to Day 21 a steady growth phase was seen for cells grown in standard media or ZnO_2, however higher cell metabolic activity was recorded for cells grown in CeZnO_5 and ZrZnO_5. A similar pattern was observed for days 14, 21 and 28. These particles likely improved the cell proliferation rate over the 28-day period. The cells did attach and proliferate in the presence of CuZnO_5 and no adhesion impairment or cell death (based on cell metabolic activity data) was observed for up to 28 days (Fig. 17 B). Tukey's multiple comparison test confirmed that the ZrZnO_5 improved cell metabolic activity by 17% higher than the standard media and 4% higher than ZnO_2.

The presence of another phase while performing doping is considered unsuccessful (failure to obtain a phase pure ceramic particles)
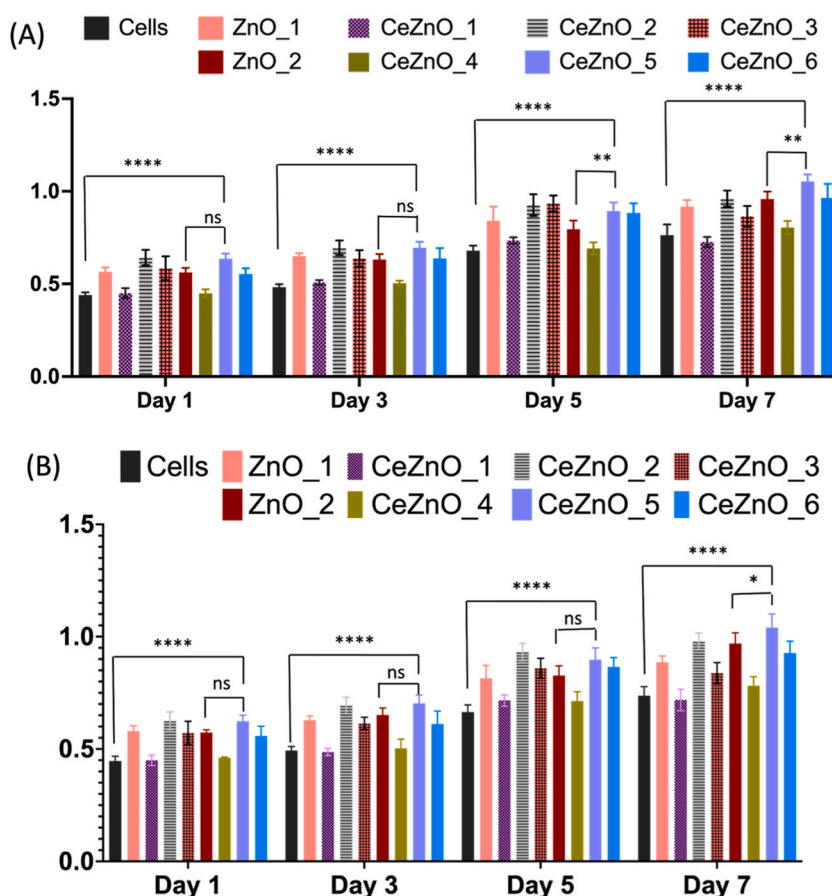
Fig. 14. 7-Day cell viability assay using nanoparticle suspension (Absorbance λ 370 nm). (A) 5 μg/ml nanoparticle suspension. (B) 10 μg/ml nanoparticle suspension. Data represents $\pm$ mean SD, n = 3*3, * = p < 0.05.

however, in the current research the presence of another phase such as CeO$_2$ and CuO was found not to inhibit biological activity. The cell metabolic activity was higher for cells in CeZnO_5 and CuZnO_5 as compared ZnO_2. CeO$_2$ nanoparticles were reported to facilitate cell proliferation and differentiation of human mesenchymal stem cells (hMSCs) because CeO$_2$ nanoparticles act as a free radical scavenger when loaded in low concentrations. CeO$_2$ is in trivalent state which is more stable and acts as antioxidant which plays an important role in enhanced cell proliferation. When free radicals are generated within the cells they interfere with the cells' normal growth. The superoxide radicals when in contact with CeO$_2$ are converted into peroxides, such peroxides attached to the surface of CeO$_2$ more strongly that the oxygen molecule. In this way, CeO$_2$ nanoparticles regulate oxygen within the cells which is the key factor for cell growth and proliferation [53].

Cu+/Cu+2 in low concentrations is reported to be safe for cell culture. a burst release of copper from scaffolds can reduce or impair cell proliferation and induce cell toxicity, however low concentrations stimulate endothelial cells [54]. Cu ions were reported to enhance recruitment and cross linking of tropoelastin precursors and promote mature fibre formation. Low levels of Cu ions induce vascularisation however 10-fold increase in ion levels i.e. 560 ng of Cu+2 promotes wound tissue ingrowth. Cu ions are known to facilitate the release of growth factors and cytokines which help the proliferation of mesenchymal cells, towards osteogenic differentiation [55]. Copper ions and Zn ions are very important for enzymatic functions, copper containing proteins involved in normal functioning of enzymes work in three different ways. Electron transfer reactions such as DNA repair, oxygen transport and storage and transport of metals. copper is responsible for bone metabolism and turnover. It is also involved in collagen fibre deposition and angiogenesis [56].

The higher cell numbers in the presence of ZrZnO_5 might be associated with higher adsorption of proteins such as fibronectin. Because ZrZnO_5 might have lower negative zeta potential as compared to pure ZnO_2 hence causing less repulsion. Fibronectin and vitronectin are crucial extracellular proteins that control cell behaviours such as adhesion, migration and differentiation [57]. The adhesion of these proteins is very important for cell attachment as it leads to cells spreading and morphological adaptation to the substrates that the proteins are attached to Refs. [58,59].
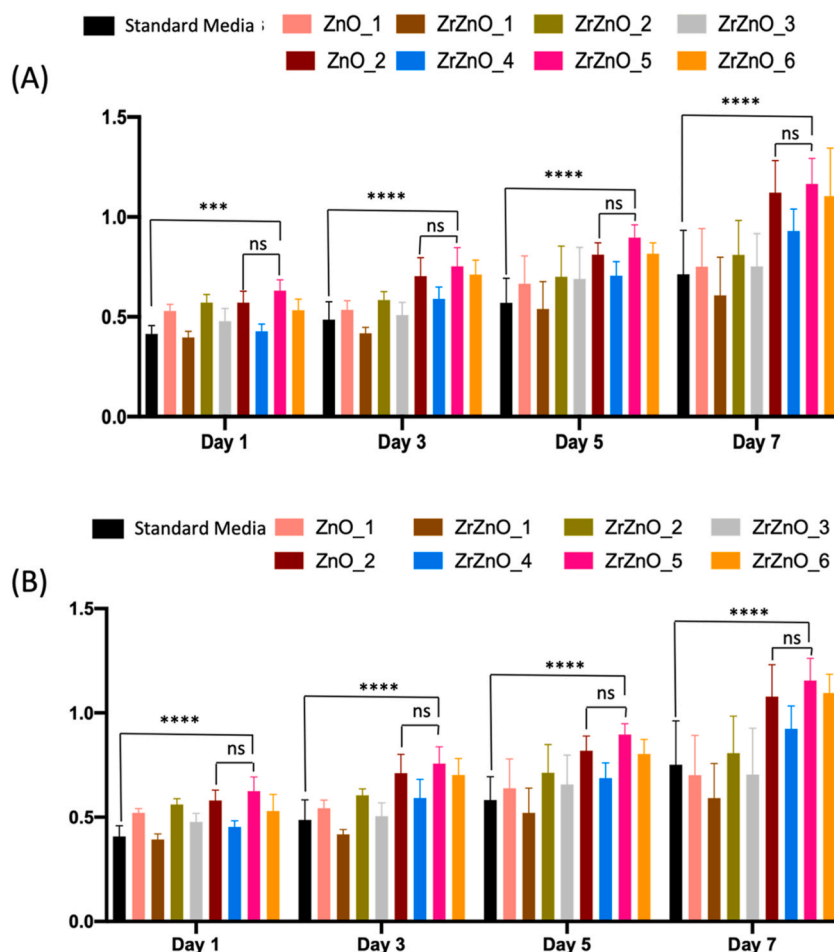
Fig. 15. Cell Metabolic Activity of MG63 cultured in zirconium doped ZnO nanoparticle media suspension A)5 μg/ml, B) 10 μg/ml, expressed with absorbance units, mean ± S.D, n = 3, N = 3, **** = p < 0.0001. (Absorbance λ 370 nm).

4. Conclusion

The flow synthesis of ZnO is a relatively new approach to synthesis specially for tissue engineering application. Reports in literature rely on complex synthesis methods which are expensive and time consuming. The current study demonstrated the flow synthesis system for synthesis of cerium, zirconium, and copper doped zinc oxide for tissue engineering applications. The results suggested that the successful synthesis of zirconium doped ZnO, however, cerium and copper doping resulted in appearance of secondary phases such as CeO_2 and CuO. The introduction of Zirconium, copper, and cerium during ZnO synthesis resulted in functionally improved ZnO nanoparticles when introduced to preliminary cell viability assay. The zirconium doped ZnO nanoparticles showed highest cell metabolic activity as compared to Phase pure ZnO or standard media controls. Which concluded that the doping resulted in functional improvement hence enhancing the cell attachment and proliferation. No cell inhibition or detachment was observed for ZrZnO_5, the cells proliferated well for up to 28 days. Importantly the hES-MPs cells that represent the cells a bone biomaterial would encounter in vivo proliferated well in presence of ZrZnO_5. The current data demonstrated successful synthesis of functionally improved ZnO nanoparticles and concluded that the ionic dopings especially zirconium doping result in unique nanoparticles which can improve overall biological properties. ZrZnO_5 holds a potential for use in tissue engineering applications such as composite membranes, guided bone regenerative membranes, 3-dimensional porous scaffolds and electrospun fibres for the applications of soft and hard tissue regeneration.

Data availability statement

Data is included in article/referenced in article. For inquiries or assistance regarding data please contact hafsahakhtar@cuilahore.edu.pk.
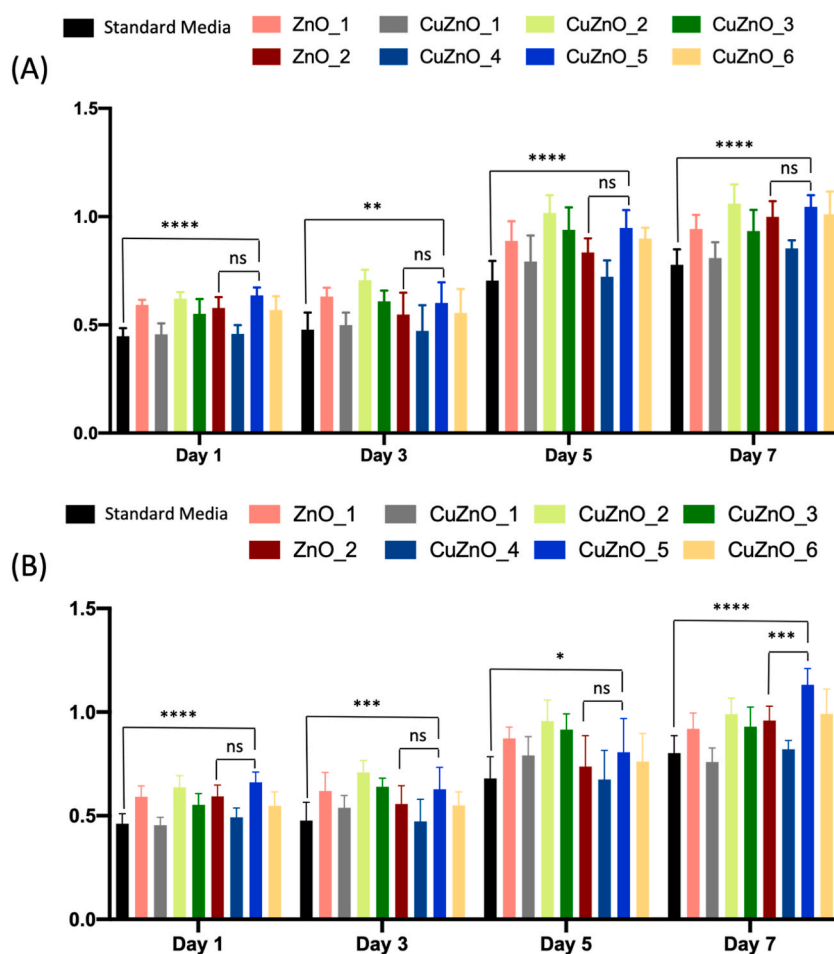
Fig. 16. *Metabolic Activity of MG63 cultured in nanoparticle media suspension (A)(5 μg/ml),(B) (10 μg/ml), expressed as resazurin absorbance units, mean etc at Day 1, 3, 5 and 7. Data represents mean ± S.D, n=3, N=3, *= p<0.05. (Absorbance λ 370 nm).*
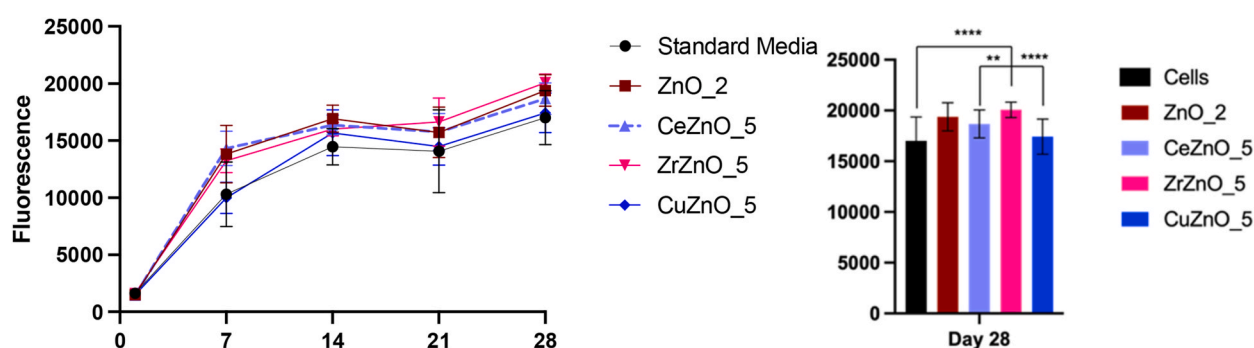
Fig. 17. (A) Metabolic Activity of hES-MP cells cultured in nanoparticle media suspension. (10 μg/ml), expressed with fluorescent units at Day 1, 7, 14, 21 and 28 days. (B) Only Day 28 data is shown and difference between cell metabolic activity of ZrZnO_5 was shown relative to control, CeZnO_5 and CuZnO_5 mean +S.D, n = 3, N = 3. *= p<0.05.

CRediT authorship contribution statement

Hafsah Akhtar: Writing – original draft, Project administration, Methodology, Funding acquisition, Data curation, Conceptualization. **Fahad Hussain Alhamoudi:** Writing – original draft, Investigation, Funding acquisition. **Julie Marshall:** Resources, Methodology. **Thomas Ashton:** Methodology. **Jawwad A. Darr:** Funding aquisition and Methodology. **Ihtesham Ur Rehman:**

Supervision. **Aqif Anwar Chaudhry:** Data curation. **Gwendolen Reilly:** Writing – review & editing, Supervision, Project administration, Methodology, Funding acquisition, Conceptualization.

Declaration of competing interest

Acknowledgements

References

[1] M. Abd-Ellah, et al., Plasmonic gold nanoparticles for ZnO-nanotube photoanodes in dye-sensitized solar cell application, Nanoscale 8 (3) (2016) 1658–1664.
[2] D. Calestani, et al., Growth of ZnO tetrapods for nanostructure-based gas sensors, Sens. Actuators, B 144 (2) (2010) 472–478.
[3] P. Chen, L. Gu, X. Xue, Y. Song, L. Zhu, X. Cao, Facile synthesis of highly uniform ZnO multipods as the supports of Au and Ag nanoparticles, Mater. Chem. Phys. 122 (1) (2010) 41–48.
[4] R. Gazia, et al., An easy method for the room-temperature growth of spongelike nanostructured Zn films as initial step for the fabrication of nanostructured ZnO, Thin Solid Films 524 (2012) 107–112.
[5] M. Laurenti, A. Verna, M. Fontana, M. Quaglio, S. Porro, Selective growth of ZnO nanowires on substrates patterned by photolithography and inkjet printing, Appl. Phys. 117 (2) (2014) 901–907.
[6] C. Pacholski, A. Kornowski, H. Weller, Self-assembly of ZnO: from nanodots to nanorods, Angew. Chem. Int. Ed. 41 (7) (2002) 1188–1191.
[7] R. Shi, et al., Growth of flower-like ZnO via surfactant-free hydrothermal synthesis on ITO substrate at low temperature, CrystEngComm 14 (18) (2012) 5996–6003.
[8] B. Baruwati, D.K. Kumar, S. V Manorama, Hydrothermal synthesis of highly crystalline ZnO nanoparticles: a competitive sensor for LPG and EtOH, Sens. Actuators, B 119 (2) (2006) 676–682.
[9] B. Dumontel, et al., Enhanced biostability and cellular uptake of zinc oxide nanocrystals shielded with a phospholipid bilayer, J. Mater. Chem. B 5 (44) (2017) 8799–8813.
[10] A.E. Kandjani, M.F. Tabriz, B. Pourabbas, Sonochemical synthesis of ZnO nanoparticles: the effect of temperature and sonication power, Mater. Res. Bull. 43 (3) (2008) 645–654.
[11] L. Shahzadi, et al., Development of K-doped ZnO nanoparticles encapsulated crosslinked chitosan based new membranes to stimulate angiogenesis in tissue engineered skin grafts, Int. J. Biol. Macromol. 120 (2018) 721–728.
[12] A.M. Deliormanlı, Synthesis and characterization of cerium-and gallium-containing borate bioactive glass scaffolds for bone tissue engineering, J. Mater. Sci. Mater. Med. 26 (2) (2015) 67.
[13] S. Shruti, A.J. Salinas, G. Lusvardi, G. Malavasi, L. Menabue, M. Vallet-Regi, Mesoporous bioactive scaffolds prepared with cerium-, gallium-and zinc-containing glasses, Acta Biomater. 9 (1) (2013) 4836–4844.
[14] T. Tosiriwatanapong, W. Singhatanadgit, Zirconia-based biomaterials for hard tissue reconstruction, Bone Tissue Regen. Insights 9 (2018) 1179061X18767886.
[15] N. Sinha, G. Ray, S. Bhandari, S. Godara, B. Kumar, Synthesis and enhanced properties of cerium doped ZnO nanorods, Ceram. Int. 40 (8) (2014) 12337–12342.
[16] A.J. Kulandaisamy, V. Elavalagan, P. Shankar, G.K. Mani, K.J. Babu, J.B.B. Rayappan, Nanostructured Cerium-doped ZnO thin film–A breath sensor, Ceram. Int. 42 (16) (2016) 18289–18295.
[17] G.N. Dar, et al., Ce-doped ZnO nanorods for the detection of hazardous chemical, Sens. Actuators, B 173 (2012) 72–78.
[18] J. Yang, et al., Low-temperature growth and optical properties of Ce-doped ZnO nanorods, Appl. Surf. Sci. 255 (5) (2008) 2646–2650.
[19] M. Yousefi, M. Amiri, R. Azimirad, A.Z. Moshfegh, Enhanced photoelectrochemical activity of Ce doped ZnO nanocomposite thin films under visible light, J. Electroanal. Chem. 661 (1) (2011) 106–112.
[20] M. Rezaei, A. Habibi-Yangjeh, Simple and large scale refluxing method for preparation of Ce-doped ZnO nanostructures as highly efficient photocatalyst, Appl. Surf. Sci. 265 (2013) 591–596.
[21] K.M. Shafi, R. Vinodkumar, R.J. Bose, V.N. Uvais, V.P.M. Pillai, Effect of Cu on the microstructure and electrical properties of Cu/ZnO thin films, J. Alloys Compd. 551 (2013) 243–248.
[22] S.-H. An, T. Matsumoto, H. Miyajima, A. Nakahira, K.-H. Kim, S. Imazato, Porous zirconia/hydroxyapatite scaffolds for bone reconstruction, Dent. Mater. 28 (12) (2012) 1221–1231.
[23] B. Chouchene, et al., High performance Ce-doped ZnO nanorods for sunlight-driven photocatalysis, Beilstein J. Nanotechnol. 7 (2016) 1338.
[24] R.S. Zeferino, M.B. Flores, U. Pal, Photoluminescence and Raman scattering in Ag-doped ZnO nanoparticles, J. Appl. Phys. 109 (1) (2011) 14308.
[25] C. Bueno-Ferrer, S. Parres-Esclapez, D. Lozano-Castelló, A. Bueno-López, Relationship between surface area and crystal size of pure and doped cerium oxides, J. Rare Earths 28 (5) (2010) 647–653.
[26] J. Zhang, et al., Synthesis and magnetic properties of Zr doped ZnO Nanoparticles, Nanoscale Res. Lett. 6 (1) (2011) 587.
[27] C.-Y. Tsay, K.-S. Fan, Optimization of Zr-doped ZnO thin films prepared by sol-gel method, Mater. Trans. 49 (8) (2008) 1900–1904.
[28] S.F. Mansour, S.I. El-Dek, M.K. Ahmed, Physico-mechanical and morphological features of zirconia substituted hydroxyapatite nano crystals, Sci. Rep. 7 (2017) 43202.
[29] N. Clament Sagaya Selvam, J.J. Vijaya, L.J. Kennedy, Effects of morphology and Zr doping on structural, optical, and photocatalytic properties of ZnO nanostructures, Ind. Eng. Chem. Res. 51 (50) (2012) 16333–16345.
[30] L. Castañeda, Fabrication of transparent conductive zinc oxide Co-doped with fluorine and zirconium thin solid films by ultrasonic chemical pyrolysis: effects of precursor solution aging and substrate temperature, J. Coatings 2013 (2013).
[31] E.I. Naik, H.S.B. Naik, R. Viswanath, B.R. Kirthan, M.C. Prabhakara, Effect of zirconium doping on the structural, optical, electrochemical and antibacterial properties of ZnO nanoparticles prepared by sol-gel method, Chem. Data Collect. 29 (2020) 100505.
[32] S. Chatkaewsueb, N. Saysunee, N. Tamaekong, The synthesis and characterization of p-CuO/n-ZnO nanoparticles synthesized by chemical method, Mater. Today Proc. 4 (5) (2017) 6111–6117.